cosmetics

MDPI

Article

Sizing Lamellar Cosmetic Emulsions: Deep-Learning Image Segmentation and Laser Diffraction as Complementary Techniques

Axel Viton [1,2,*], Raphaël Coatmeur [2], Béatrice Anthouard [1], Christophe Sauzet [2], Magalie Claeys-Bruno [2,*] and Philippe Piccerelle [2]

[1] Laboratoire SICAF Cosmétiques, 367 All. Bellecour, 84200 Carpentras, France
[2] CNRS, IRD, IMBE, Avignon Université, Aix-Marseille University, 13385 Marseille, France
* Correspondence: axelviton@hotmail.fr (A.V.); m.claeys-bruno@univ-amu.fr (M.C.-B.)

Abstract

Droplet size distribution governs the stability and sensory properties of cosmetic emulsions. Many cosmetic emulsions are lamellar. Each droplet carries a birefringent shell and is a core-shell object. Laser diffraction is the usual sizing technique. Its Mie inversion requires a single refractive index. This index is poorly defined for a droplet with a lamellar shell. Optical microscopy avoids this assumption. It measures each droplet directly on the image, whatever its refractive index. Combined with image segmentation, it offers an independent sizing route. We compared laser diffraction with a classical watershed and a deep-learning model (Cellpose) on 13 lamellar emulsions imaged at ×10, ×20, and ×40. Diameters were calibrated from the instrument metadata and reweighted to volume. Cellpose and laser diffraction give the same central size. Their dv50 differ by less than 1.5 µm on all 13 emulsions at ×10. Paired tests show no significant dv50 difference at ×10 and ×40 (adjusted $p \geq 0.13$). The watershed reaches this agreement only on the coarsest emulsions. It overestimates the dv50 of the finer ones by 15 to 35% and fails at ×40. The two techniques differ only at the ends of the distribution. At the upper end, laser diffraction gives a higher dv90 than microscopy. A non-spherical laser model does not remove this gap. Possible causes are the smoothing of the laser inversion and the evolution of the sample under dilution. At the lower end, microscopy gives a higher dv10 because it does not detect droplets below its optical resolution. The same slides also reveal the lamellar shell under crossed polarizers. Deep-learning microscopy is thus a quantitative sizing method for the central size of lamellar emulsions. The two techniques are complementary for the characterization of lamellar emulsions.

Keywords: lamellar emulsion; droplet size distribution; laser diffraction; optical microscopy; image segmentation; Cellpose; watershed

Check for updates

Academic Editor: Enzo Berardesca

Received: 9 October 2026
Revised: 10 November 2026
Accepted: 11 November 2026
Published: 19 November 2026

Copyright: © 2026 by the authors. Licensee MDPI, Basel, Switzerland. This article is an open access article distributed under the terms and conditions of the Creative Commons Attribution (CC BY) license.

1. Introduction

The droplet size distribution (DSD) is a primary quality attribute of emulsions. It controls creaming and coalescence kinetics, bulk rheology and, in cosmetic products, sensory texture [1–3]. Reliable, cross-validated DSD measurement is therefore central to formulation and process development. It relies on two complementary measurement families. The first is ensemble light scattering, dominated by laser diffraction. The second is direct imaging by optical microscopy. Each family relies on its own physical principle and its own model. The next two paragraphs introduce them in turn. We chose these two families because they

cover the micrometric size range of cosmetic emulsions and the equipment of a formulation laboratory. Photon correlation spectroscopy is designed for sub-micrometer particles and is poorly suited to broad micrometric distributions. Electron microscopy requires fixation or cryo-preparation of soft lamellar droplets, and its throughput is too low to size hundreds of thousands of droplets.

Laser diffraction (LD) is the reference technique for particle and droplet sizing. It is fast, samples the whole population, and returns a volume-weighted distribution over a very wide dynamic range [4]. It is most firmly established for dry, solid powders. It is applied less routinely to liquid dispersions such as emulsions. Its accuracy rests on two assumptions. Scatterers are spherical, homogeneous and non-interacting, with a single refractive index, following Mie theory. The size distribution is recovered by inverting the scattering pattern.

Optical microscopy provides the complementary direct view. Individual droplets are imaged and measured. This gives a number-weighted read-out and morphological information. Its drawbacks are a smaller sampled volume and the 2D projection of 3D objects. Historically, manual counting was also laborious, which motivates automated image segmentation [5,6]. Classical segmentation, such as thresholding and the marker-controlled watershed, is fast and transparent. But it struggles with dense, touching, polydisperse droplets. Learning-based segmentation, and generalist deep-learning models in particular [7,8], have become strong tools for round cell-like objects. Their behavior on emulsion droplets and how it compares to a classical baseline and to LD is not well documented.

The emulsions of interest here add a structural complication. Lamellar gel networks are commonly used in cosmetic and pharmaceutical creams [9–14]. Many cosmetic systems, and ours in particular, are stabilized by a glucoside/fatty-alcohol surfactant that builds a lamellar phase at the oil-water interface [10,15]. Each droplet is then a core-shell object: an oil core wrapped in an ordered, birefringent shell whose refractive index differs from the core. Two consequences follow. For laser diffraction, the single-refractive-index, homogeneous-sphere premise of the Mie inversion no longer holds strictly, and the instrument is blind to the shell it inverts through. The refractive index required by the inversion is then poorly defined. That inversion is also an ill-posed, regularized problem, so the returned distribution is smoothed. For optical microscopy, crossed polarizers turn the shell into a positive signal: birefringent droplets light up against a dark field, often with the characteristic Maltese cross, so the same imaging route that sizes the droplets can also read their lamellar organization.

A point rarely stated is that the microscopy result also depends on the magnification. A low magnification samples a large field but resolves fine droplets poorly. A high magnification resolves fine droplets but samples a small field and changes the radiometry of the image. The magnification is usually chosen once and left implicit, so its effect on the reported size is hidden.

Prior work has begun to close the microscopy-versus-LD gap. Microscopy image analysis has already been compared to laser diffraction for emulsions. Trainable Weka Segmentation found microscopy percentiles slightly above LD [16]. Confocal microscopy has also been compared with laser diffraction for milk fat globules [17]. Classical and deep-learning segmenters have been benchmarked on emulsion micrographs [18,19]. Deep learning has also been applied to droplet sizing in flow and microfluidic contexts [20,21], and a machine-learning detector trained on synthetic images has been reported to remain consistent with laser diffraction in liquid–liquid systems [22]. Image analysis has also been compared with PDPA and laser diffraction on sprays [23]. These comparisons targeted food or generic industrial emulsions, all treated as homogeneous spheres. To our knowledge, none has addressed a lamellar cosmetic emulsion, where each droplet is a birefringent core-shell object.

As a result, no study has compared laser diffraction with both a classical watershed and a deep-learning pipeline on the same lamellar samples and on a common volume basis. A generalist deep-learning segmenter [7] is not yet established for emulsion droplets. Its behavior across magnifications is also unknown. This study therefore asks two practical questions. First, do optical-microscopy image analysis and laser diffraction converge on the size of a core-shell birefringent droplet, and where and why do the two diverge? Second, which segmentation route is the more trustworthy across magnifications, classical watershed or deep learning? To answer them, we size the same thirteen emulsions by all three techniques at three magnifications. We reconcile the sizing on a common volume-weighted basis. We treat the magnification as an explicit study axis rather than a fixed setting. The emulsions used come from a study of the homogenization conditions, a factor that directly shifts droplet size. We took advantage of this series, which spans a wide range of droplet sizes, to test the three techniques on the same samples. The effect of the process itself is not analyzed here, so that the study remains focused on the comparison of the techniques.

2. Materials and Methods

Answering these questions requires the three techniques to be applied to identical material, then brought onto a single comparable basis. Figure 1 gives the overall analysis architecture. This section describes the emulsions, then the two measurement routes, laser diffraction and optical microscopy; the microscopy route covers image acquisition and calibration and the two segmentation pipelines, classical watershed and the deep-learning model, with manual annotation. It closes with the framework that reconciles the number-weighted image data with the volume-weighted laser data, and with the polarized-light protocol used to probe the lamellar shell.

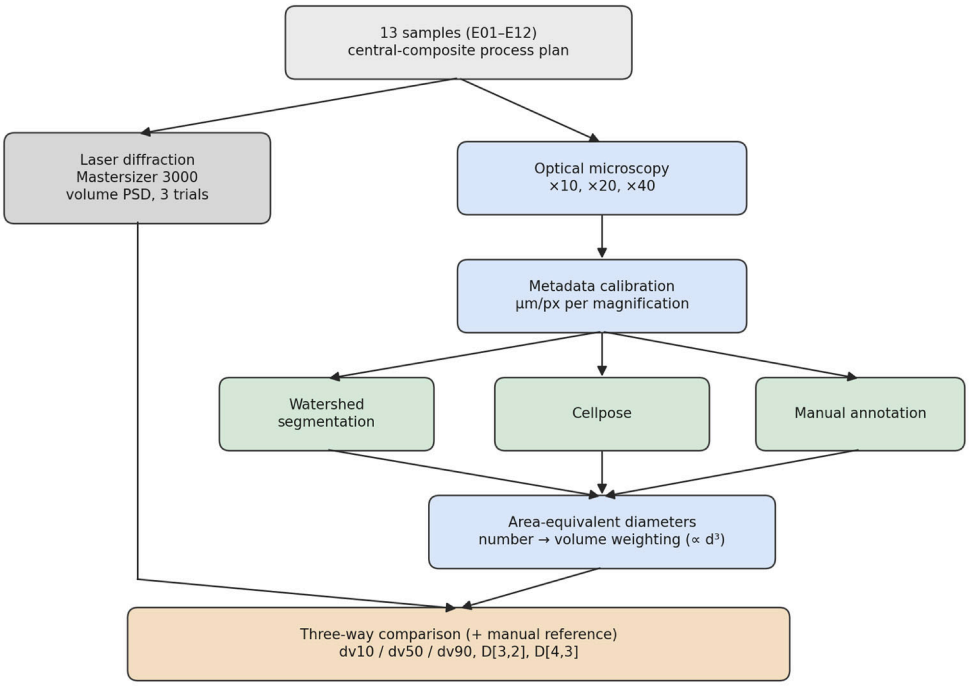

Figure 1. Analysis architecture: the 13 samples are measured by laser diffraction and by optical microscopy (×10/×20/×40); microscopy is calibrated from the metadata, segmented by watershed and Cellpose, reweighted to volume, and the three routes are compared. A manual annotation (about fifty droplets per field) is kept as a human reference.

2.1. Emulsions

Thirteen oil-in-water emulsions of the same base composition were produced. E5′1 and E5′2 are a repeated experiment: the same process condition was prepared twice, independently, which gives an inter-batch reproducibility point. The emulsions share one base formulation and differ only in their process conditions. These were varied to document how the process shifts droplet size. The emulsions were produced at different homogenization conditions for this purpose: rotor speed (1000 to 3000 rpm) and mixing time (5 to 15 min) combined across thirteen runs, one condition being repeated (E5′1 and E5′2, Table 1). We do not attempt a full design-of-experiments analysis.

Table 1. The 13 emulsions and their process conditions (rotor speed and mixing time). E5′1 and E5′2 are two independent preparations under the same process conditions.

Sample	Rotor Speed (rpm)	Mixing Time (min)
E1	1000	5
E2	3000	5
E3	1000	15
E4	3000	15
E5′1	1000	10
E5′2	1000	10
E6	3000	10
E7	2000	5
E8	2000	15
E9	2000	10
E10	1567	8.75
E11	2433	8.75
E12	2000	12.5

The base is a simple oil-in-water emulsion, emulsified on a VMI MULTILAB ML03 pilot mixer (VMI, Montaigu-Vendée, France). The oil phase is Labrafac CC (Gattefossé, Saint-Priest, France; INCI: Caprylic/Capric Triglyceride) at 20%, emulsified with Montanov 202 at 5% (SEPPIC, Paris, France; INCI: Arachidyl Alcohol, Behenyl Alcohol, Arachidyl Glucoside). This glucoside/fatty-alcohol system builds the lamellar network probed later by polarized light. The formulation is stabilized with Solagum AX at 0.4% (SEPPIC, Paris, France; INCI: Acacia Senegal Gum, Xanthan Gum) and preserved with Sepicide HB at 1.5% (SEPPIC, Paris, France; INCI: Phenoxyethanol, Methylparaben, Ethylparaben, Propylparaben, Butylparaben). The aqueous phase is water (q.s. 100%), with glycerin at 1% as a humectant.

2.2. Laser Diffraction Analysis

The thirteen samples share one composition and differ only in their process conditions, which gives a wide range of droplet sizes on a single chemistry. They were first measured by laser diffraction.

Laser diffraction was performed on a Mastersizer 3000 (Malvern Instruments Ltd., Worcestershire, UK). The refractive index of the dispersing water phase was 1.33. The refractive index of the emulsion was 1.4401, measured on the emulsion fatty phase with an Anton Paar Abbemat 300 refractometer (Anton Paar GmbH, Graz, Austria).

A hydro dispersion module dispersed the droplets. The dispersion speed was about 1300 rpm, adjusted to emulsion viscosity and stability. The obscuration was kept between 8% and 20%. This range is high enough to give a stable signal, yet low enough to avoid multiple scattering. The instrument returns the volume-weighted distribution over 100 logarithmically spaced classes, from 0.01 to 3300 µm.

Each sample was measured in three trials of six scans. The reference distribution for each sample is the mean over the three trials. The volume percentiles dv10, dv50, and dv90 were computed from the cumulative volume distribution. The median coefficient of variation on the dv50 is 1.0%, so the laser measurement is stable at the sample level.

2.3. Optical Microscopy

Laser diffraction gives an ensemble, volume-weighted distribution but does not see individual droplets. The same samples were therefore imaged by optical microscopy. Microscopy adds the direct, number-weighted view. It covers image acquisition and calibration, then the two segmentation pipelines, classical watershed and the deep-learning model.

2.3.1. Image Acquisition and Calibration

Droplet morphology was imaged by bright-field transmitted-light microscopy on a Leica DM4B microscope (Leica Microsystems, Wetzlar, Germany) with Leica N PLAN dry objectives (Leica Microsystems, Wetzlar, Germany; ×10 NA 0.25, ×20 NA 0.40, ×40 NA 0.65). Samples were prepared as thin films between glass slides. Images were acquired with the Leica acquisition software (version 3.7) in standard mode, at 6.3 megapixels and 3072 × 2048 px. The exposure time was 250 ms, and the gain was 1.00. Transmitted-light intensity was optimized at diaphragm aperture 14 and TL-Fld 27. Colorimetric settings were standardized across acquisitions, with software white balance, fixed channel offsets, and a saturation of 62.

Magnification is treated here as an explicit study axis. Each sample was imaged at ×10, ×20, and ×40, plus a ×10 acquisition under crossed polarizers. The sampling plan is complete and without gaps: 13 samples × 3 slides × 5 fields × 4 modalities, 780 images in total. On each slide, the five fields were taken at the center and at the edge of the slide, to cover the spatial variation of the film.

The spatial calibration of the images depended on the objective used. Observations performed with the ×10 objective, under both transmitted light and polarized light (LP), shared the same pixel size of 0.43965 µm/px, since the polarizing filters do not alter the optical magnification. Switching to the ×20 objective reduced the pixel size to 0.21843 µm/px, and the ×40 objective further decreased it to 0.10886 µm/px. Pixel size was read directly from the Leica acquisition metadata as the physical field size divided by the pixel count. The value is unique.

2.3.2. Watershed Segmentation

Two edge cues were combined into an elevation surface. A local background was estimated by Gaussian smoothing ($\sigma = 6.4$ µm) and subtracted from the grayscale image, giving a ring map in which the dark rims surrounding each droplet take positive values. This ring map was combined with the Sobel gradient magnitude by pixelwise maximum. The result is a surface with high values along droplet boundaries. Watershed markers were placed on bright droplet interiors. Local maxima of the lightly smoothed greyscale image (Gaussian $\sigma = 0.85$ µm) were detected with a minimum inter-seed distance of 2.56 µm and an absolute intensity threshold of 0.20, restricted to pixels away from any rim. Each maximum seeded one label. The watershed transform [24] was flooded from these markers over the elevation surface. Regions were retained on four joint criteria: eccentricity ≤ 0.80, solidity ≥ 0.90, mean intensity ≥ 0.35, and area above the objective-specific detection limit. This limit is set by optical resolution, not by an arbitrary pixel floor. The Rayleigh criterion, $d = 0.61 \cdot \lambda / NA$ at $\lambda = 0.55$ µm, gives detection limits of 1.34, 0.84, and 0.52 µm at ×10, ×20, and ×40. Each magnification therefore resolves down to its own optical limit, with the ×40 objective accessing fine droplets below the ×10 limit. This is the rationale for the

multi-magnification design. At every magnification, the limit corresponds to 3 to 5 px, so the images are simultaneously well-sampled and diffraction-limited. For each retained region, the area-equivalent diameter was computed and converted to micrometers with the magnification-specific calibration reported above. The pipeline was implemented with scikit-image 0.26.0 [6]. The watershed relies on hand-tuned edge and intensity cues, which makes it sensitive to image contrast and droplet density. The same images were therefore also segmented with a deep-learning model that learns the object boundaries instead.

2.3.3. Deep-Learning Model

Droplets were also segmented with Cellpose [7], a generalist deep-learning model for instance segmentation. Cellpose does not predict masks directly. A U-Net backbone predicts, at each pixel, a spatial gradient field pointing toward the center of the object it belongs to, together with a foreground probability. Individual masks are then recovered by following these gradients to their convergence points, which separates touching objects without a hand-tuned edge model. We used Cellpose 3.1.1.2 [25] with the pretrained cyto model [7], without retraining. The field was passed as a single grayscale channel (channels = [0, 0]), with the droplets playing the role of the cytoplasm the model was trained on.

Cellpose resizes each image so that the expected object diameter matches the ~30 px scale the model was trained at. This is the role of the diameter parameter, and it is why a single call is tuned to one size scale. Our code therefore does not rely on Cellpose autoscaling. It runs the model once per value of a fixed sweep, [10, 25, 50, 100, 200] px, and fuses the passes. Each pass is stored on disk so that a field is segmented once and reused. From each returned label map, objects are extracted by region analysis with scikit-image and at the objective-specific resolution limit, and their area-equivalent diameters are converted to micrometers. Inference used the Cellpose package on GPU; deduplication and fusion were implemented in NumPy 2.5.4. The other Cellpose parameters were left at their default values.

2.3.4. Manual Annotation Protocol

Both automated pipelines return tens to hundreds of thousands of droplets per sample, but neither is validated against a human reading. A manual annotation was therefore performed on a subset of the same fields. As an algorithm-independent check, droplets were also outlined by hand. On one representative field per sample and per magnification, about fifty droplets were fitted with a circle, using the same metadata calibration and the same volume reweighting and threshold as the automated pipelines. It samples tens of droplets, whereas the automated pipelines sample tens to hundreds of thousands, so it is a human check on what the segmentations detect, not a technique on equal footing. The annotation consists of fitted circles, not pixel masks, so segmentation metrics such as the intersection over union, the Dice coefficient, precision, and recall cannot be computed from it. Extending it to a number of droplets large enough for stable volume percentiles was not feasible: the dataset holds 780 images and up to 286,288 droplets per sample, and a serious annotation would take several days of work per magnification. In a preliminary and unpublished work, Cellpose was also compared with manual annotation on selected individual droplets.

2.4. Comparison Framework

Laser diffraction is volume-weighted; microscopy is number-weighted. To compare them, image diameters were reweighted to volume ($\propto d^3$). Because volume weighting scales as the cube of the diameter, a single large droplet outweighs about a thousand fine ones, so

the reweighting is what makes the number-based image data comparable to the volume-based laser data. Diameters were pooled over the three slides and five fields of each sample before computing percentiles, because the between-field variability of the coarse tail exceeds the between-slide variability (see the reproducibility results in Sections 3.2.1 and 3.2.2). For the comparison, all techniques were truncated to a common lower bound of 1.67 µm, set above the coarsest optical resolution (the ×10 objective, 1.34 µm), so that the three routes are read over the same measurement domain. The descriptors are defined as follows.

For each segmented object of projected area A_i, the area-equivalent diameter is:

$$d_i = 2\sqrt{\frac{A_i}{\pi}} \tag{1}$$

Each droplet is then weighted by its volume, assuming a sphere of diameter d_i:

$$w_i = \frac{d_i^3}{\sum_j d_j^3} \tag{2}$$

The percentiles dv10, dv50, and dv90 are the diameters at which the cumulative volume fraction reaches 10, 50, and 90%.

The moment means are defined as:

$$D[p,q] = \frac{\sum_i d_i^p}{\sum_i d_i^q} \tag{3}$$

with $D[3,2]$ the Sauter mean and $D[4,3]$ the De Brouckere mean.

The width of the distribution is given by:

$$\text{span} = \frac{dv90 - dv10}{dv50} \tag{4}$$

2.5. Polarized-Light Imaging

The ×10 acquisition under crossed polarizers gives 195 fields (13 samples × 3 slides × 5 fields), on the same metadata calibration. Droplets coated by a lamellar shell are birefringent. They appear bright on a dark background, often showing the characteristic Maltese cross.

2.6. Statistical Analysis

Each image method was compared with laser diffraction for each descriptor (dv10, dv50, dv90, $D[3,2]$ and $D[4,3]$) and each magnification, over the 13 emulsions (E5′1 and E5′2 counted as two preparations). The relative difference to the laser value was computed for each emulsion. Paired differences were tested with an exact two-sided Wilcoxon signed-rank test, and the p values were adjusted with the Holm method over the 15 comparisons made for each segmentation method. Agreement was also described by Bland-Altman analysis on the logarithm of the ratio between the image value and the laser value, reported as a percent bias with limits of agreement (Figure S1, Supplementary Materials).

3. Results

The results follow the microscopy workflow: the laser measurement first, then the two segmentation pipelines read as distributions and summary tables, and a final three-method comparison. Every results table reports dv10, dv50, dv90, the Sauter mean $D[3,2]$, the De Brouckere mean $D[4,3]$, and the span $(\text{dv90} - \text{dv10})/\text{dv50}$.

3.1. Laser Diffraction

Laser diffraction was applied to all 13 samples. Every sample gives a unimodal distribution over the measured range, with a single mode, as shown in Figure 2. The dv50 spans from 6.5 µm for E4 to 16.9 µm for E5′2. Four groups appear in this descriptor. E1, E3, E5′1, and E5′2 are the coarsest, between 16.1 and 16.9 µm. E1, E3, and E5′1 lie within 0.2 µm of each other, and E5′2 sits 0.8 µm above E5′1. E10 stands alone at 13.4 µm. E7 and E9 follow at 11.6 and 11.0 µm. E12, E8, E11, and E2 form a close group between 8.4 and 9.9 µm. E4 and E6 are the finest, at 6.5 and 6.8 µm.

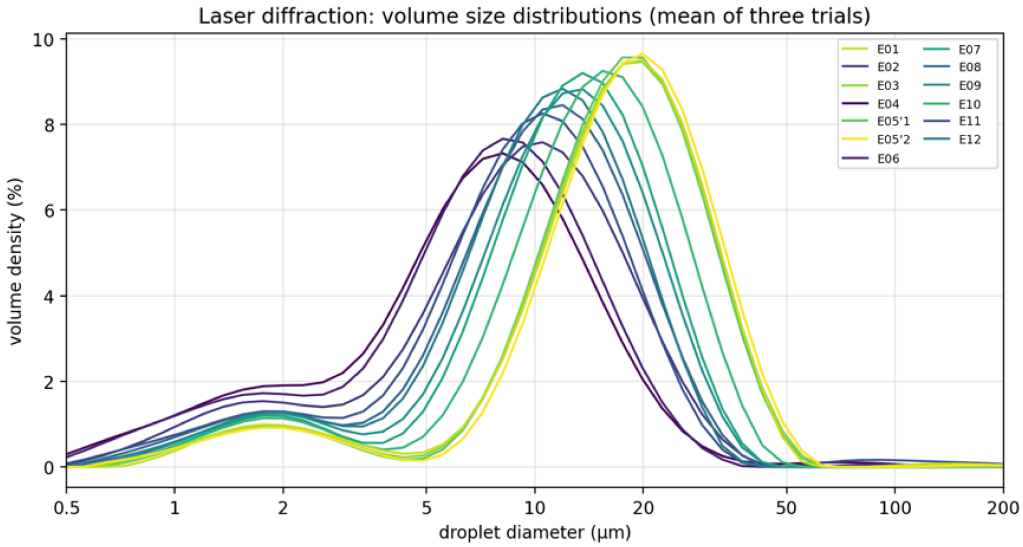

Figure 2. Laser diffraction: volume size distributions of the 13 samples (mean of three trials), colored from the finest (purple) to the coarsest (yellow) by dv50. Colors encode the dv50 rank, so samples with close dv50 (here E4 and E6) appear in similar colors.

The other percentiles follow the same ranking. The dv10 ranges from 1.5 µm for E4 to 6.6 µm for E5′2. It stays between 5.8 and 6.6 µm for the coarse group and falls below 2 µm for E2, E4, and E6. The dv90 ranges from 14.8 µm for E4 and E6 to 31.3 µm for E5′2. It stays between 29.7 and 31.7 µm for the coarse group across all trials. The dv10 varies more between samples than the dv50: it changes by a factor of about four between the finest and the coarsest samples, against a factor of about 2.5 for the dv50. The finest samples therefore carry a proportionally larger fine fraction. This appears directly in the span, which increases as the dv50 decreases. The coarse group has the narrowest distributions, with a span between 1.46 and 1.50. The intermediate samples lie between 1.60 and 1.75. E11 reaches 1.82, and E2, E4, and E6 are the widest, between 1.94 and 2.06.

The mean diameters confirm these trends. $D[3,2]$ ranges from 3.9 µm for E4 to 9.4 µm for E1 and E5′2. $D[4,3]$ ranges from 8.4 µm for E6 to 19.6 µm for E5′2. For every sample, $D[4,3]$ lies above the dv50 by about 2.5 µm for the coarse group and 2 µm for E4 and E6. The ratio $D[4,3]/D[3,2]$ is close to 2.0 for the coarse group and slightly higher, 2.1 to 2.2, for the finest samples, in line with their wider span.

Each sample was measured in three trials of six scans, reported in Table 2. The three trials agree closely on the dv50. The largest difference between trials is 0.5 µm, on E5′2, and the median coefficient of variation is 1.0%. With a Student distribution for three trials, the between-trial 95% confidence interval is ±0.45 µm on the dv10, ±0.33 µm on the dv50, and ±0.70 µm on the dv90. The dv10 is less repeatable on the intermediate samples. On E7 and E10, the first trial reads a dv10 above the other two by 1.1 to 1.2 µm. The same trend affects $D[3,2]$, which is highest in the first trial on all 13 samples. The dv90 differs by less

than 1 µm between trials, except on E1 with 1.4 µm and E11 with 2.1 µm. $D[4,3]$ is the least repeatable descriptor because it is the most sensitive to a few large objects. The second trial of E7 gives a $D[4,3]$ of 28.4 µm, against 13.4 and 13.2 µm for the other two, while its dv90 remains unchanged. This isolated value is treated as an outlier. The third trial of E10 and the trials of E11 also show $D[4,3]$ differences of 1.8 to 3.0 µm. The span stays repeatable, with differences below 0.17 between trials on every sample.

Table 2. Laser-diffraction summary, all thirteen samples in columns. For each descriptor, the three trials (T1, T2, T3) are on separate rows, followed by the between-trial standard deviation σ ($n = 3$) (volume-weighted, µm; span dimensionless).

Descriptor	E1	E2	E3	E4	E5′1	E5′2	E6	E7	E8	E9	E10	E11	E12
dv10 (T1)	5.9	2.1	5.8	1.6	6.4	6.4	1.7	4.2	2.8	3.2	4.4	2.4	2.8
dv10 (T2)	5.8	1.9	6.0	1.4	6.4	6.6	1.5	3.0	2.3	2.8	3.3	2.2	2.5
dv10 (T3)	5.8	1.7	6.2	1.5	6.0	6.8	1.5	3.0	2.4	2.5	3.7	2.2	2.6
dv10 (σ)	0.1	0.2	0.2	0.1	0.2	0.2	0.1	0.7	0.3	0.4	0.6	0.1	0.2
dv50 (T1)	16.4	8.4	16.0	6.6	15.9	16.6	7.0	11.7	9.7	11.1	13.3	9.1	9.9
dv50 (T2)	16.1	8.4	16.2	6.5	16.2	17.0	6.7	11.6	9.6	11.0	13.4	8.8	9.9
dv50 (T3)	16.3	8.3	16.3	6.4	16.1	17.1	6.7	11.5	9.7	10.8	13.5	8.9	9.9
dv50 (σ)	0.2	0.1	0.2	0.1	0.2	0.3	0.2	0.1	0.1	0.2	0.1	0.2	0.0
dv90 (T1)	31.1	18.0	29.9	14.7	29.2	30.8	15.1	22.0	19.3	21.5	24.9	19.6	18.9
dv90 (T2)	29.7	18.3	29.9	15.1	30.1	31.4	14.7	22.2	19.4	21.5	25.2	17.5	19.5
dv90 (T3)	29.7	18.7	30.3	14.7	30.2	31.7	14.7	21.9	19.4	21.0	25.6	18.4	19.3
dv90 (σ)	0.8	0.4	0.2	0.2	0.6	0.5	0.2	0.2	0.1	0.3	0.4	1.1	0.3
$D[3,2]$ (T1)	9.5	5.3	9.2	4.0	9.6	9.5	4.4	7.7	6.2	7.1	8.2	5.7	6.4
$D[3,2]$ (T2)	9.5	5.1	9.0	3.8	9.2	9.2	4.0	7.0	5.7	6.7	7.6	5.3	6.1
$D[3,2]$ (T3)	9.3	4.7	9.1	3.8	9.0	9.3	3.9	7.0	5.8	6.3	7.8	5.3	6.1
$D[3,2]$ (σ)	0.1	0.3	0.1	0.1	0.3	0.2	0.3	0.4	0.3	0.4	0.3	0.2	0.2
$D[4,3]$ (T1)	20.0	10.1	18.2	8.1	18.1	18.9	8.5	13.4	11.3	12.8	15.1	13.2	11.3
$D[4,3]$ (T2)	18.2	10.2	18.3	8.7	19.3	19.7	8.1	28.4	11.3	13.0	15.2	10.2	11.5
$D[4,3]$ (T3)	18.3	10.8	18.8	8.6	19.0	20.3	8.4	13.2	11.3	12.4	17.0	11.9	11.4
$D[4,3]$ (σ)	1.0	0.4	0.3	0.3	0.6	0.7	0.2	8.7	0.0	0.3	1.1	1.5	0.1
span (T1)	1.54	1.88	1.51	2.00	1.43	1.47	1.90	1.53	1.71	1.65	1.55	1.89	1.63
span (T2)	1.48	1.95	1.48	2.10	1.46	1.46	1.96	1.66	1.78	1.70	1.64	1.75	1.70
span (T3)	1.47	2.05	1.48	2.07	1.50	1.46	1.96	1.64	1.76	1.72	1.62	1.83	1.69
span (σ)	0.04	0.09	0.02	0.05	0.04	0.01	0.03	0.07	0.04	0.04	0.05	0.07	0.04

Laser diffraction thus provides a stable measurement for the thirteen samples. The distributions are unimodal, the dv50 spans 6.5 to 16.9 µm, and the samples fall into distinct size groups. The three trials agree closely, with a median coefficient of variation of 1.0% on the dv50. Only the volume-weighted mean $D[4,3]$ shows a single extreme trial, on E7, which illustrates how strongly a few large objects weigh on a volume-based descriptor. This trial results from a single scan containing a transient mode between 1 and 3 mm, attributed to an air bubble or a foreign particle; the five other scans of this trial give 13.1 µm, in line with trials 1 and 3. No scan was removed: the mean over the three trials is used for every sample, which explains the large standard deviation of the $D[4,3]$ of E7. The distributions are also wide, with a span of 1.46 to 2.06, and the finest samples (E2, E4, E6) are the widest. This measurement rests, however, on the Mie model, which treats each droplet as a homogeneous sphere with a single refractive index. Its values are therefore compared below with the diameters measured directly by image analysis.

3.2. Microscopy Image Analysis

The two segmentation pipelines are read side by side before they are judged. Figure 3 shows, for each sample, the original ×20 micrograph next to the watershed and the Cellpose segmentation of the same field. On the fine emulsions (E2, E4, E6), Cellpose fills the field

where the watershed leaves gaps; on the coarse ones, the two agree visually. Each pipeline is then read as a volume distribution and a summary table.

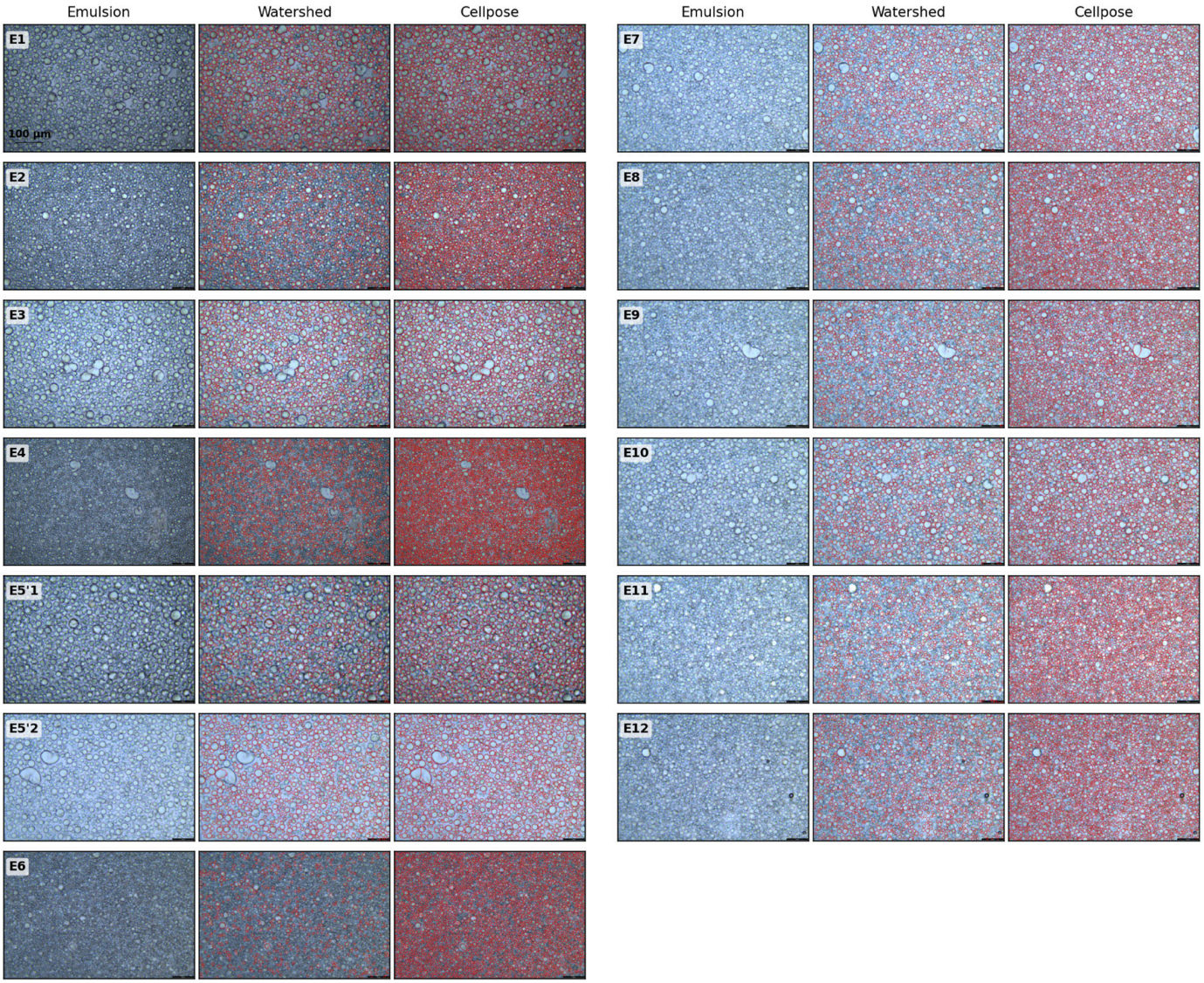

Figure 3. Segmentation of the 13 samples at ×20 (full field). For each sample (E1 to E12; E5′1 and E5′2 are the two preparations of the same condition), the panels show the original micrograph (**left**), the marker-controlled watershed (**middle**), and Cellpose (**right**). Red outlines are the detected droplet boundaries on the image. (E1) 1000 rpm, 5 min; (E2) 3000 rpm, 5 min; (E3) 1000 rpm, 15 min; (E4) 3000 rpm, 15 min; (E5′1) 1000 rpm, 10 min; (E5′2) 1000 rpm, 10 min; (E6) 3000 rpm, 10 min; (E7) 2000 rpm, 5 min; (E8) 2000 rpm, 15 min; (E9) 2000 rpm, 10 min; (E10) 1567 rpm, 8.75 min; (E11) 2433 rpm, 8.75 min; (E12) 2000 rpm, 12.5 min (process conditions as in Table 1). Scale bar: 100 µm (shown in the E1 panel; same scale in all panels).

3.2.1. Classical Watershed

The watershed returns unimodal distributions for all 13 samples (Figure 4). Table 3 gives the resulting diameters at the three magnifications. At ×10, the samples fall into four groups by dv50. The coarsest are E1, E3, E5′1, E5′2, and E10, with dv50 between 15.6 and 16.8 µm. E7, E9, and E12 follow, between 12.3 and 13.6 µm. E2, E8, and E11 lie between 10.2 and 11.7 µm. E4 and E6 are the finest, at 8.3 and 8.7 µm. E1 and E3 give almost identical values on every descriptor. So do E5′1 and E5′2 at ×10.

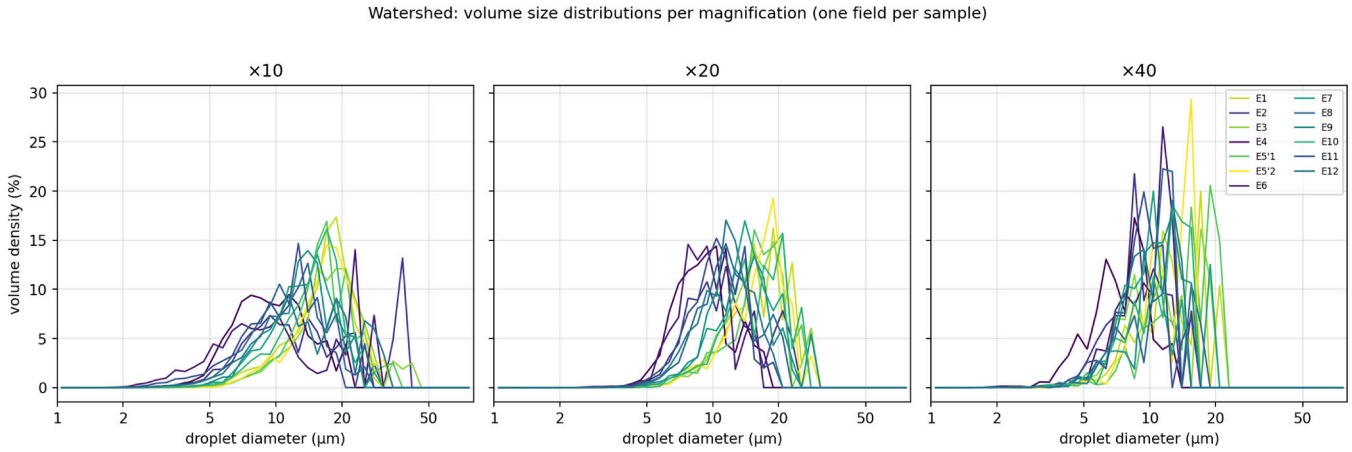

Figure 4. Watershed volume size distributions of the 13 samples at ×10, ×20 and ×40 (one field per sample), colored from the finest (purple) to the coarsest (yellow) by dv50. Colors encode the dv50 rank, so samples with close dv50 (here E1, E3, E5′1 and E5′2) appear in similar colors.

The ×10 and ×20 magnifications give close dv50 values. The difference never exceeds 1.3 µm. It is slightly positive for the coarse samples E1, E3, E5′1, E5′2 and slightly negative for the intermediate ones E7, E9, E12, E2, E8. The ranking of the samples is the same at both magnifications. At ×40, all diameters decrease. The decrease grows with droplet size. For the coarse samples, dv50 drops by 2.6 to 4.5 µm relative to ×10 (E1 from 16.7 to 12.2 µm). For E7, E9, E12, and E2, it drops by about 2 to 3 µm. For the finest samples, it is small: 0.6 µm for E4 and 0.2 µm for E6. The dv50 scale therefore narrows at ×40, from 8.3 to 16.8 µm at ×10 down to 7.7 to 13.6 µm. The coarse group stays on top, but its internal order changes. The intermediate group E7, E9, E12 merges with E2, E8, and E11, all between 9.4 and 10.8 µm.

The tails of the distributions respond differently to magnification. For the coarse samples, dv10 and dv90 are stable between ×10 and ×20 (about 10 and 23 µm), and both decrease at ×40 (about 7.5 and 18 to 20 µm). For the fine samples, the effect is concentrated on dv90. It decreases steadily with magnification: from 16.7 to 13.7, then 10.9 µm for E4, and from 21.3 to 17.1, then 13.1 µm for E2. Their dv10, in contrast, is lowest at ×10 and rises at ×20 before stabilizing at E11: 5.4, 6.8, and 6.6 µm. At ×10, the fine distributions are therefore wider at both ends.

The span follows the same logic. For the coarse samples, it stays close to 0.8 at ×10 and ×20 and increases at ×40 (up to 1.01 for E5′2). For the fine samples, it is highest at ×10, between 1.08 and 1.37, and falls to 0.71 to 0.75 at ×40. The intermediate samples E7, E9, and E10 show their widest span at ×20. At ×40, the fine samples reach the narrowest distributions of the whole set. The mean diameters agree with these trends. For the coarse samples, $D[4,3]$ is close to dv50, and $D[3,2]$ is about 2 µm lower at every magnification. For the fine samples at ×10, $D[4,3]$ exceeds dv50 by 1.5 µm (E4, E2), which reflects the weight of the coarse tail. This gap disappears at ×40, where $D[4,3]$ and dv50 differ by less than 0.3 µm.

Reproducibility was assessed at two levels, between fields and between slides. The between-field dispersion exceeds the between-slide dispersion. A single field does not contain enough large droplets to define the coarse tail. The fields of each slide are therefore pooled before computing the percentiles. With this pooling, the between-slide standard deviation on dv50 stays below 1 µm in 36 of the 39 sample and magnification pairs. The exceptions are E10 at ×20 (1.2 µm) and ×40 (2.9 µm) and E5′1 at ×40 (1.2 µm). E10 at ×40 is the least reproducible case for every descriptor. dv90 is the most dispersed percentile. Its standard deviation reaches 3.8 to 5.2 µm for E2, E4, and E6 at ×10, which also carry the

largest span deviations (0.37 to 0.60). The same samples become reproducible at ×20 and ×40, with dv90 deviations below 1.6 µm. dv10 is the most robust descriptor, with deviations of 0.3 µm or less outside the fine samples at ×10. The same fields were then segmented with Cellpose to test whether a deep-learning model reduces this dependence on magnification.

Table 3. Watershed results at ×10, ×20, and ×40 (volume-weighted, µm; span dimensionless), mean over the three slides. Values are the mean ± between-slide standard deviation ($n = 3$ slides).

Sample	Mag.	dv10	dv50	dv90	$D[3,2]$	$D[4,3]$	Span
E1	×10	9.7 ± 0.2	16.7 ± 0.4	23.1 ± 0.9	14.7 ± 0.4	16.6 ± 0.5	0.80 ± 0.03
	×20	10.0 ± 0.3	17.6 ± 0.4	24.1 ± 0.9	15.4 ± 0.4	17.4 ± 0.4	0.80 ± 0.02
	×40	7.4 ± 0.1	12.2 ± 0.5	18.8 ± 1.3	11.1 ± 0.3	12.7 ± 0.5	0.93 ± 0.11
E2	×10	6.4 ± 0.6	11.3 ± 0.1	21.3 ± 3.8	10.2 ± 0.4	12.8 ± 0.8	1.32 ± 0.37
	×20	6.7 ± 0.2	10.4 ± 0.7	17.1 ± 1.6	9.8 ± 0.4	11.3 ± 0.4	1.01 ± 0.17
	×40	6.2 ± 0.1	9.4 ± 0.2	13.1 ± 0.8	8.7 ± 0.2	9.5 ± 0.3	0.73 ± 0.07
E3	×10	9.6 ± 0.1	16.6 ± 0.1	22.6 ± 0.1	14.7 ± 0.1	16.4 ± 0.1	0.78 ± 0.01
	×20	9.8 ± 0.0	17.2 ± 0.3	23.4 ± 0.5	15.1 ± 0.1	17.0 ± 0.2	0.80 ± 0.02
	×40	7.4 ± 0.2	12.5 ± 0.3	17.8 ± 0.8	11.2 ± 0.1	12.6 ± 0.1	0.82 ± 0.10
E4	×10	5.4 ± 0.6	8.3 ± 0.6	16.7 ± 4.7	8.0 ± 0.2	9.8 ± 1.6	1.37 ± 0.49
	×20	5.7 ± 0.2	8.4 ± 0.3	13.7 ± 1.6	8.1 ± 0.3	9.2 ± 0.6	0.94 ± 0.17
	×40	5.1 ± 0.4	7.7 ± 0.3	10.9 ± 0.2	7.2 ± 0.3	7.9 ± 0.3	0.75 ± 0.06
E5′1	×10	9.7 ± 0.1	16.2 ± 0.6	22.9 ± 0.7	14.6 ± 0.4	16.4 ± 0.4	0.81 ± 0.03
	×20	9.9 ± 0.3	16.7 ± 0.6	23.1 ± 1.4	14.9 ± 0.5	16.7 ± 0.6	0.79 ± 0.08
	×40	7.9 ± 0.9	13.6 ± 1.2	19.4 ± 1.2	12.1 ± 0.9	13.7 ± 0.6	0.84 ± 0.23
E5′2	×10	9.7 ± 0.2	16.8 ± 0.3	23.2 ± 0.6	14.9 ± 0.3	16.7 ± 0.4	0.81 ± 0.01
	×20	10.1 ± 0.2	18.0 ± 0.6	24.0 ± 0.6	15.7 ± 0.1	17.7 ± 0.2	0.77 ± 0.02
	×40	7.6 ± 0.3	12.7 ± 0.6	20.4 ± 1.5	11.5 ± 0.6	13.4 ± 0.8	1.01 ± 0.05
E6	×10	5.4 ± 0.9	8.7 ± 0.4	15.4 ± 5.2	8.1 ± 0.4	9.7 ± 1.3	1.15 ± 0.60
	×20	6.2 ± 0.1	8.9 ± 0.1	13.4 ± 0.6	8.6 ± 0.1	9.8 ± 0.5	0.80 ± 0.06
	×40	5.6 ± 0.4	8.5 ± 0.3	11.9 ± 0.4	7.8 ± 0.3	8.6 ± 0.3	0.75 ± 0.03
E7	×10	8.1 ± 0.1	13.6 ± 0.2	19.4 ± 0.1	12.2 ± 0.1	13.8 ± 0.1	0.82 ± 0.02
	×20	8.2 ± 0.2	13.4 ± 0.4	20.6 ± 0.1	12.3 ± 0.2	14.0 ± 0.2	0.93 ± 0.03
	×40	6.7 ± 0.3	10.7 ± 0.3	16.1 ± 1.3	9.8 ± 0.3	11.1 ± 0.2	0.87 ± 0.16
E8	×10	6.7 ± 1.4	11.7 ± 0.9	19.4 ± 1.7	10.3 ± 1.4	12.5 ± 1.1	1.08 ± 0.06
	×20	7.3 ± 0.0	10.9 ± 0.3	16.8 ± 1.8	10.4 ± 0.2	11.6 ± 0.5	0.87 ± 0.14
	×40	7.0 ± 0.1	10.4 ± 0.2	14.4 ± 1.0	9.7 ± 0.3	10.6 ± 0.4	0.71 ± 0.07
E9	×10	7.7 ± 0.2	12.9 ± 0.3	19.2 ± 0.5	11.6 ± 0.4	13.2 ± 0.3	0.89 ± 0.01
	×20	7.8 ± 0.2	12.4 ± 0.4	20.2 ± 1.1	11.7 ± 0.3	13.5 ± 0.3	1.00 ± 0.07
	×40	7.0 ± 0.2	10.8 ± 0.3	15.3 ± 0.4	10.0 ± 0.3	11.0 ± 0.3	0.77 ± 0.01
E10	×10	8.8 ± 0.7	15.6 ± 0.8	21.8 ± 1.2	13.5 ± 1.1	15.5 ± 0.9	0.84 ± 0.01
	×20	8.7 ± 0.4	14.9 ± 1.2	22.7 ± 1.9	13.4 ± 0.8	15.4 ± 1.1	0.94 ± 0.07
	×40	7.5 ± 1.3	12.5 ± 2.9	18.9 ± 3.6	11.4 ± 2.2	12.9 ± 2.6	0.92 ± 0.04
E11	×10	5.4 ± 0.5	10.2 ± 0.7	16.8 ± 2.1	8.8 ± 0.8	11.0 ± 1.1	1.12 ± 0.10
	×20	6.8 ± 0.0	10.0 ± 0.1	14.8 ± 0.3	9.6 ± 0.1	10.5 ± 0.2	0.80 ± 0.03
	×40	6.6 ± 0.1	9.7 ± 0.1	13.6 ± 0.4	9.1 ± 0.0	10.0 ± 0.1	0.73 ± 0.06
E12	×10	7.3 ± 0.1	12.3 ± 0.1	20.9 ± 2.1	11.2 ± 0.1	13.3 ± 0.2	1.11 ± 0.18
	×20	7.5 ± 0.1	11.4 ± 0.2	18.7 ± 1.2	10.9 ± 0.2	12.5 ± 0.3	0.99 ± 0.09
	×40	6.8 ± 0.1	10.1 ± 0.2	14.2 ± 0.8	9.5 ± 0.2	10.3 ± 0.3	0.73 ± 0.06

3.2.2. Deep-Learning Model (Cellpose)

Cellpose is run as a multi-diameter sweep. The passes are fused on inter-magnification coherence, and the retained rule is auto + fine. The segmentation returns unimodal distributions for all 13 samples (Figure 5). Table 4 gives the resulting diameters at the three magnifications. At ×10, Cellpose sizes range from 98,500 to 286,288 droplets per sample, pooled over the fifteen fields, against 47,077 to 77,396 for the watershed. At ×10, the samples

fall into four groups by dv50. E1, E3, E5′1, and E5′2 are the coarsest, between 16.4 and 17.1 µm. E10, E7, and E9 follow, between 11.6 and 13.5 µm. E12 and E8 lie at 9.9 and 9.4 µm. E2, E4, E6, and E11 are the finest, between 7.7 and 8.7 µm. E1 and E3 give almost identical values on every descriptor. So do E5′1 and E5′2.

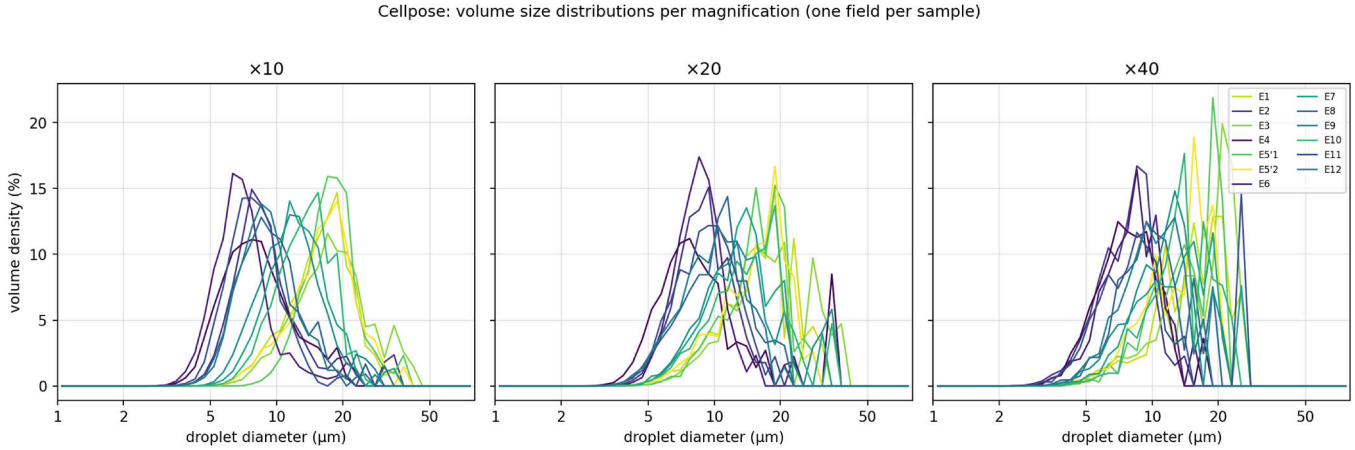

Figure 5. Cellpose (auto + fine) volume size distributions of the 13 samples at ×10, ×20, and ×40 (one field per sample), colored from the finest (purple) to the coarsest (yellow) by dv50. Colors encode the dv50 rank, so samples with close dv50 (here E1, E3, E5′1 and E5′2) appear in similar colors.

The dv50 is little affected by magnification. For every sample, the three values stay within 1.6 µm of each other. The four groups hold at ×10, ×20, and ×40. The coarse samples show a slight decrease with magnification, of 0.5 to 1.6 µm between ×10 and ×40 (E5′1 from 17.1 to 15.5 µm). E7 and E9 follow the same slight trend. E10 is the only sample whose dv50 rises, from 13.5 to 14.1 µm. The fine samples and E8 and E12 show their highest dv50 at ×20. The effect is largest for E11, which moves from 8.0 µm at ×10 to 9.6 µm at ×20 and back to 8.7 µm at ×40. The dv50 scale is nearly unchanged across magnifications, from 7.7 to 17.1 µm at ×10 and from 7.3 to 16.2 µm at ×40.

The tails respond more to magnification than the median. For the coarse samples, dv10 decreases steadily, by 1.6 to 1.9 µm between ×10 and ×40 (E1: 10.5, 9.4, and 8.7 µm). Their dv90 stays between 22 and 26 µm and peaks at ×20 for three of the four samples. For the fine samples, dv10 rises at ×20 and falls again at ×40 (E11: 5.3, 6.5, and 5.2 µm). The lowest dv10 of the set is 4.6 µm (E6 at ×40). The dv90 of E2, E4, and E6 decreases with magnification, most markedly for E4 (16.9, 13.0, and 11.4 µm). The dv90 of E8, E11, and E12 instead peaks at ×20. E10 is again the exception, with a dv90 that increases slightly from 20.4 to 21.8 µm.

The span shows opposite trends for the coarse and fine samples. For the coarse samples, it is lowest at ×10 (0.78 to 0.88) and rises to about 0.9 at ×20 and ×40, following the decrease of dv10. For the fine samples, it is highest at ×10, up to 1.49 for E4 and 1.12 to 1.14 for E6 and E2, and falls at ×20. At ×40, all spans lie between 0.82 and 0.96. The intermediate samples keep a span close to 0.9 at every magnification. The mean diameters agree with these trends. For the coarse samples, $D[4,3]$ exceeds dv50 by 0.1 to 1.1 µm, and $D[3,2]$ is 1.2 to 2.2 µm lower, with the widest gap at ×40. For E2, E4, and E6 at ×10, $D[4,3]$ exceeds dv50 by 1.2 to 1.6 µm. This gap shrinks to 0.4 to 0.6 µm at ×40.

Reproducibility was assessed at two levels, between fields and between slides. The between-field dispersion exceeds the between-slide dispersion. The fields of each slide are therefore pooled before computing the percentiles. The between-slide standard deviation on dv50 stays below 1 µm in 36 of the 39 sample and magnification pairs. Its median is 0.3 µm. The three exceptions are all at ×10: E4, E6, and E10. dv90 is the most dispersed

percentile, with standard deviations of 4.7 µm for E4 and 3.3 µm for E6 at ×10. These two samples also carry the largest span deviations (0.37 and 0.21). E10 at ×10 is dispersed on every descriptor, yet it becomes one of the most reproducible cases at ×40, with deviations of 0.3 µm or less. More generally, ×40 is the most reproducible magnification. All dv50 deviations stay at or below 0.8 µm, all dv90 deviations at or below 1.4 µm, and all span deviations at or below 0.09. Cellpose keeps the same four size groups and a nearly constant dv50 across the three magnifications. The two automated pipelines were finally checked against a manual annotation of the same fields.

Table 4. Cellpose (auto + fine) results at ×10, ×20 and ×40 (volume-weighted, µm; span dimensionless), mean over the three slides. Values are mean ± between-slide standard deviation ($n = 3$ slides).

Sample	Mag.	dv10	dv50	dv90	$D[3,2]$	$D[4,3]$	Span
E1	×10	10.5 ± 0.2	16.6 ± 0.1	23.6 ± 0.4	15.2 ± 0.2	17.1 ± 0.4	0.79 ± 0.01
	×20	9.4 ± 0.5	16.6 ± 0.8	24.7 ± 0.8	14.6 ± 0.7	17.0 ± 0.8	0.92 ± 0.02
	×40	8.7 ± 0.5	15.9 ± 0.2	23.3 ± 0.3	13.7 ± 0.4	16.0 ± 0.4	0.91 ± 0.02
E2	×10	5.5 ± 0.2	8.7 ± 0.6	15.4 ± 1.2	8.3 ± 0.5	9.9 ± 0.7	1.14 ± 0.03
	×20	6.1 ± 0.2	9.1 ± 0.1	14.4 ± 0.5	8.7 ± 0.1	10.0 ± 0.1	0.91 ± 0.09
	×40	5.2 ± 0.3	8.6 ± 0.4	13.5 ± 1.4	7.9 ± 0.5	9.2 ± 0.7	0.96 ± 0.09
E3	×10	10.3 ± 0.1	16.4 ± 0.1	24.7 ± 1.0	15.1 ± 0.1	17.5 ± 0.4	0.88 ± 0.06
	×20	9.3 ± 0.1	16.5 ± 0.3	25.6 ± 0.4	14.6 ± 0.2	17.2 ± 0.3	0.99 ± 0.04
	×40	8.9 ± 0.2	16.0 ± 0.8	23.5 ± 1.2	13.9 ± 0.6	16.2 ± 0.8	0.92 ± 0.05
E4	×10	5.0 ± 0.4	8.0 ± 1.2	16.9 ± 4.7	7.8 ± 1.0	9.6 ± 1.6	1.49 ± 0.37
	×20	5.2 ± 0.1	7.9 ± 0.2	13.0 ± 1.1	7.5 ± 0.2	8.8 ± 0.3	1.00 ± 0.14
	×40	4.7 ± 0.3	7.3 ± 0.5	11.4 ± 0.9	6.8 ± 0.5	7.8 ± 0.5	0.92 ± 0.02
E5′1	×10	10.9 ± 0.4	17.1 ± 0.4	24.3 ± 0.2	15.8 ± 0.4	17.9 ± 0.3	0.78 ± 0.03
	×20	9.5 ± 0.2	16.4 ± 0.2	23.8 ± 0.5	14.6 ± 0.2	16.8 ± 0.1	0.87 ± 0.04
	×40	9.0 ± 0.1	15.5 ± 0.8	22.2 ± 0.8	13.6 ± 0.3	15.6 ± 0.5	0.85 ± 0.02
E5′2	×10	10.7 ± 0.3	16.9 ± 0.3	24.8 ± 0.8	15.6 ± 0.4	18.0 ± 0.7	0.83 ± 0.02
	×20	9.6 ± 0.1	16.9 ± 0.2	25.2 ± 0.7	15.0 ± 0.2	17.5 ± 0.4	0.92 ± 0.04
	×40	8.7 ± 0.1	16.2 ± 0.1	24.0 ± 0.6	13.9 ± 0.1	16.3 ± 0.1	0.95 ± 0.04
E6	×10	5.1 ± 0.5	7.7 ± 1.2	13.7 ± 3.3	7.5 ± 1.0	8.9 ± 1.5	1.12 ± 0.21
	×20	5.7 ± 0.1	8.4 ± 0.2	12.3 ± 1.9	8.0 ± 0.2	9.1 ± 0.8	0.79 ± 0.21
	×40	4.6 ± 0.1	7.5 ± 0.4	11.3 ± 1.1	6.9 ± 0.3	7.9 ± 0.5	0.89 ± 0.08
E7	×10	7.9 ± 0.3	12.4 ± 0.2	18.3 ± 0.1	11.5 ± 0.3	13.2 ± 0.3	0.84 ± 0.03
	×20	7.8 ± 0.1	12.2 ± 0.2	19.1 ± 0.5	11.4 ± 0.2	13.2 ± 0.3	0.93 ± 0.02
	×40	7.0 ± 0.2	12.1 ± 0.4	18.4 ± 0.2	10.8 ± 0.1	12.5 ± 0.2	0.94 ± 0.01
E8	×10	6.0 ± 0.4	9.4 ± 0.6	15.1 ± 1.2	8.9 ± 0.5	10.3 ± 0.7	0.96 ± 0.04
	×20	6.8 ± 0.0	10.4 ± 0.1	15.9 ± 0.7	9.8 ± 0.1	11.0 ± 0.3	0.87 ± 0.06
	×40	6.1 ± 0.3	10.0 ± 0.3	14.9 ± 0.7	9.1 ± 0.3	10.3 ± 0.3	0.87 ± 0.04
E9	×10	7.3 ± 0.3	11.6 ± 0.5	17.3 ± 1.1	10.8 ± 0.5	12.4 ± 0.8	0.87 ± 0.03
	×20	7.3 ± 0.1	11.4 ± 0.2	18.1 ± 0.5	10.8 ± 0.2	12.4 ± 0.3	0.95 ± 0.01
	×40	6.7 ± 0.1	10.9 ± 0.1	17.3 ± 0.1	10.1 ± 0.1	11.7 ± 0.2	0.96 ± 0.02
E10	×10	8.1 ± 0.9	13.5 ± 1.3	20.4 ± 2.5	12.3 ± 1.2	14.3 ± 1.6	0.91 ± 0.04
	×20	8.3 ± 0.3	13.7 ± 0.6	21.2 ± 1.1	12.5 ± 0.5	14.4 ± 0.8	0.94 ± 0.02
	×40	8.4 ± 0.1	14.1 ± 0.3	21.8 ± 0.2	12.7 ± 0.1	14.7 ± 0.1	0.94 ± 0.03
E11	×10	5.3 ± 0.2	8.0 ± 0.2	12.2 ± 0.4	7.7 ± 0.2	8.6 ± 0.3	0.86 ± 0.01
	×20	6.5 ± 0.1	9.6 ± 0.1	13.7 ± 0.3	9.0 ± 0.1	9.9 ± 0.2	0.76 ± 0.02
	×40	5.2 ± 0.2	8.7 ± 0.3	12.4 ± 0.6	7.8 ± 0.3	8.9 ± 0.4	0.82 ± 0.02
E12	×10	6.2 ± 0.3	9.9 ± 0.6	15.9 ± 0.7	9.3 ± 0.5	10.8 ± 0.5	0.98 ± 0.03
	×20	7.0 ± 0.1	10.7 ± 0.2	16.8 ± 0.6	10.1 ± 0.2	11.6 ± 0.3	0.92 ± 0.05
	×40	6.5 ± 0.1	10.3 ± 0.3	15.9 ± 0.5	9.5 ± 0.3	10.9 ± 0.4	0.92 ± 0.02

3.2.3. Manual Annotation

About fifty droplets per field were outlined by hand on one field per sample and magnification, on the same calibration and volume reweighting as the automated pipelines. The route is small: it samples tens of droplets, where the segmentation size is tens to hundreds of thousands. Table 5 gives its volume percentiles for the thirteen samples at the three magnifications.

Table 5. Manual annotation results at ×10, ×20 and ×40 (one field per sample, about fifty hand-drawn droplets per field; volume-weighted, µm; span dimensionless). No replicate standard deviation: a single field is annotated per sample and magnification.

Sample	Mag.	dv10	dv50	dv90	$D[3,2]$	$D[4,3]$	Span
E1	×10	11.8	22.1	25.5	18.0	20.4	0.62
	×20	10.1	17.4	31.5	17.4	22.0	1.23
	×40	9.8	15.4	17.7	13.6	14.8	0.51
E2	×10	10.8	20.2	27.2	17.5	20.4	0.81
	×20	6.1	11.4	12.9	9.3	10.4	0.60
	×40	5.2	8.2	11.2	7.5	8.4	0.75
E3	×10	12.7	19.4	27.3	17.8	20.1	0.75
	×20	8.8	17.1	22.1	14.6	16.6	0.77
	×40	10.0	19.1	23.7	16.8	18.9	0.72
E4	×10	6.6	11.5	15.5	10.3	11.6	0.77
	×20	5.2	8.1	13.0	7.8	9.0	0.96
	×40	5.4	7.9	10.7	7.5	8.2	0.67
E5′1	×10	12.4	19.0	26.5	18.1	20.3	0.75
	×20	12.7	20.6	27.5	18.4	20.9	0.72
	×40	10.2	20.9	32.4	18.1	23.4	1.06
E5′2	×10	12.1	20.3	27.2	18.6	20.3	0.75
	×20	11.7	20.4	26.3	18.1	20.4	0.72
	×40	8.6	16.7	20.9	13.7	15.7	0.74
E6	×10	9.5	16.7	19.7	14.1	15.8	0.62
	×20	7.8	13.2	17.4	11.8	13.1	0.73
	×40	5.7	9.2	11.6	8.2	8.9	0.65
E7	×10	11.4	18.6	27.0	17.8	20.4	0.84
	×20	9.2	13.8	18.5	13.0	14.3	0.67
	×40	8.4	16.9	25.2	14.1	18.3	0.99
E8	×10	10.3	17.1	20.1	14.8	16.3	0.58
	×20	7.3	15.2	26.4	14.2	19.4	1.26
	×40	6.4	10.3	13.5	9.4	10.2	0.68
E9	×10	11.0	17.4	27.0	16.8	19.3	0.92
	×20	9.4	16.3	28.0	15.6	20.4	1.14
	×40	8.6	14.9	20.6	13.3	15.3	0.80
E10	×10	12.5	24.1	37.6	21.2	26.8	1.04
	×20	10.2	16.9	22.5	15.1	17.0	0.73
	×40	9.5	24.0	38.1	21.6	32.4	1.19
E11	×10	8.2	16.4	20.2	13.9	16.0	0.73
	×20	6.4	13.2	17.1	10.8	12.9	0.82
	×40	6.2	11.4	13.0	9.8	10.8	0.60
E12	×10	10.7	21.1	29.8	18.3	22.3	0.91
	×20	6.8	13.7	16.3	11.2	12.7	0.69
	×40	7.1	12.1	17.6	11.2	12.7	0.87

Under d^3 weighting, the manual dv50 sits well above the laser, by +77% at ×10, +28% at ×20, and +23% at ×40. A handful of large circles dominates, while the fine population, which a human under-samples, is missing. The overestimate shrinks as the magnification rises and more fines are resolved, but even at ×40 the manual dv50 stays biased. Stable

volume percentiles need the tens to hundreds of thousands of outlines the automated routes provide, not the tens a hand annotation can draw. The manual annotation confirms that the segmentations track real droplets, but it samples too few of them to give stable volume percentiles. The comparison with laser diffraction therefore relies on the two automated segmentations.

3.3. Three-Method Comparison

No single technique gives direct access to the true droplet size distribution. Each relies on its own physical principle, its own detection range, and its own model to convert a signal into a size. For a lamellar emulsion, their agreement is therefore a cross-validation of two independent routes, not the calibration of one against the other. This section identifies where laser diffraction and the two segmentations agree, and why they differ. Table 6 gathers the descriptors of the three techniques at ×10 for the thirteen samples.

The manual annotation is not included in this comparison. With about fifty outlines per field, its volume percentiles are dominated by a few large droplets. It serves only as a qualitative check that the segmentations track real droplets.

The dv50 is the descriptor on which laser diffraction and Cellpose agree best. At ×10, Cellpose falls within 1.5 µm of the laser on all 13 samples, over a range from 6.5 to 16.9 µm. The largest deviation is on E4, the finest emulsion. The watershed does not reach this agreement. It matches the laser within 0.4 µm on the four coarsest samples only—E1, E3, E5′1, E5′2—where droplets are large and well separated. On the nine others, it reads 1.3 to 2.9 µm above the laser, an overestimate of 15 to 35%. At ×40 it fails, because the brighter field defeats the intensity-based seeding. The agreement of Cellpose is notable, because the laser models each droplet as a homogeneous sphere with a single refractive index, which a lamellar droplet is not. The center survives this approximation because the droplets are large compared with the wavelength. Over the dv50 range, the size parameter $x = \pi d/\lambda$ exceeds 30 for both light sources of the instrument (632.8 and 470 nm). In this regime, the forward scattering pattern is set mainly by the geometric cross-section of the droplet and only weakly by its internal index [4].

The dv10 is where the techniques differ most, and the difference comes from their detection range. Laser diffraction covers the submicron range. Microscopy is bounded by the optical resolution of each objective, and droplets below this limit are not detected. The microscopy dv10 is therefore higher than the laser value on every sample. This loss of fines also explains the slight excess of the microscopy dv50 on the finest samples. The limit is intrinsic to optical microscopy. A higher magnification recovers part of the fine population, but at the cost of a smaller sampled field. Submicron droplets remain out of reach at every magnification used here. The Sauter mean $D[3,2]$ follows the dv10. It weights each droplet by its surface and is therefore dominated by the fine population. At ×10, the microscopy $D[3,2]$ is 1.4 to 2 times the laser value for both segmentations. The ratio is highest on the finest samples, E2, E4, and E6, where the unseen fines carry the largest share of the interface. The microscopy $D[3,2]$ preserves the ranking of the size groups. It should not, however, be read as an absolute measure of interfacial area.

Table 6. Technique summary at ×10: for each descriptor, laser diffraction, watershed, and Cellpose (auto + fine) on separate rows, the thirteen samples in columns (volume-weighted, µm; span dimensionless). Values are mean ± standard deviation: between-slide ($n = 3$ slides) for the microscopy methods, between-trial ($n = 3$) for the laser. The laser $D[4,3]$ of E7 includes trial 2 (28.4 µm), driven by a single scan with a transient coarse mode; trials 1 and 3 give 13.4 and 13.2 µm (Section 3.1).

Descriptor	Technique	E1	E2	E3	E4	E5′1	E5′2	E6	E7	E8	E9	E10	E11	E12
dv10	Laser	5.8 ± 0.1	1.9 ± 0.2	6.0 ± 0.2	1.5 ± 0.1	6.3 ± 0.2	6.6 ± 0.2	1.6 ± 0.1	3.4 ± 0.7	2.5 ± 0.3	2.8 ± 0.4	3.8 ± 0.6	2.3 ± 0.1	2.6 ± 0.2
	Watershed	9.7 ± 0.2	6.4 ± 0.6	9.6 ± 0.1	5.4 ± 0.6	9.7 ± 0.1	9.7 ± 0.2	5.4 ± 0.9	8.1 ± 0.1	6.7 ± 1.4	7.7 ± 0.2	8.8 ± 0.7	5.4 ± 0.5	7.3 ± 0.1
	Cellpose	10.5 ± 0.2	5.5 ± 0.2	10.3 ± 0.1	5.0 ± 0.4	10.9 ± 0.4	10.7 ± 0.3	5.1 ± 0.5	7.9 ± 0.3	6.0 ± 0.4	7.3 ± 0.3	8.1 ± 0.9	5.3 ± 0.2	6.2 ± 0.3
dv50	Laser	16.3 ± 0.2	8.4 ± 0.1	16.2 ± 0.2	6.5 ± 0.1	16.1 ± 0.2	16.9 ± 0.3	6.8 ± 0.2	11.6 ± 0.1	9.7 ± 0.1	11.0 ± 0.2	13.4 ± 0.1	8.9 ± 0.2	9.9 ± 0.0
	Watershed	16.7 ± 0.4	11.3 ± 0.1	16.6 ± 0.1	8.3 ± 0.6	16.2 ± 0.6	16.8 ± 0.3	8.7 ± 0.4	13.6 ± 0.2	11.7 ± 0.9	12.9 ± 0.3	15.6 ± 0.8	10.2 ± 0.7	12.3 ± 0.1
	Cellpose	16.6 ± 0.1	8.7 ± 0.6	16.4 ± 0.1	8.0 ± 1.2	17.1 ± 0.4	16.9 ± 0.3	7.7 ± 1.2	12.4 ± 0.2	9.4 ± 0.6	11.6 ± 0.5	13.5 ± 1.3	8.0 ± 0.2	9.9 ± 0.6
dv90	Laser	30.2 ± 0.8	18.3 ± 0.4	30.0 ± 0.2	14.8 ± 0.2	29.8 ± 0.6	31.3 ± 0.5	14.8 ± 0.2	22.0 ± 0.2	19.4 ± 0.1	21.3 ± 0.3	25.2 ± 0.4	18.5 ± 1.1	19.2 ± 0.3
	Watershed	23.1 ± 0.9	21.3 ± 3.8	22.6 ± 0.1	16.7 ± 4.7	22.9 ± 0.7	23.2 ± 0.6	15.4 ± 5.2	19.4 ± 0.1	19.4 ± 1.7	19.2 ± 0.5	21.8 ± 1.2	16.8 ± 2.1	20.9 ± 2.1
	Cellpose	23.6 ± 0.4	15.4 ± 1.2	24.7 ± 1.0	16.9 ± 4.7	24.3 ± 0.2	24.8 ± 0.8	13.7 ± 3.3	18.3 ± 0.1	15.1 ± 1.2	17.3 ± 1.1	20.4 ± 2.5	12.2 ± 0.4	15.9 ± 0.7
$D[3,2]$	Laser	9.4 ± 0.1	5.0 ± 0.3	9.1 ± 0.1	3.9 ± 0.1	9.2 ± 0.3	9.4 ± 0.1	4.1 ± 0.3	7.2 ± 0.4	5.9 ± 0.3	6.7 ± 0.4	7.8 ± 0.3	5.5 ± 0.2	6.2 ± 0.2
	Watershed	14.7 ± 0.4	10.2 ± 0.4	14.7 ± 0.1	8.0 ± 0.2	14.6 ± 0.4	14.9 ± 0.3	8.1 ± 0.4	12.2 ± 0.1	10.3 ± 1.4	11.6 ± 0.4	13.5 ± 1.1	8.8 ± 0.8	11.2 ± 0.1
	Cellpose	15.2 ± 0.2	8.3 ± 0.5	15.1 ± 0.1	7.8 ± 1.0	15.8 ± 0.4	15.6 ± 0.4	7.5 ± 1.0	11.5 ± 0.3	8.9 ± 0.5	10.8 ± 0.5	12.3 ± 1.2	7.7 ± 0.2	9.3 ± 0.5
$D[4,3]$	Laser	18.8 ± 1.0	10.4 ± 0.4	18.4 ± 0.3	8.5 ± 0.3	18.8 ± 0.6	19.6 ± 0.7	8.4 ± 0.2	18.3 ± 8.7	11.3 ± 0.0	12.7 ± 0.3	15.8 ± 1.1	11.8 ± 1.5	11.4 ± 0.1
	Watershed	16.6 ± 0.5	12.8 ± 0.8	16.4 ± 0.1	9.8 ± 1.6	16.4 ± 0.4	16.7 ± 0.4	9.7 ± 1.3	13.8 ± 0.1	12.5 ± 1.1	13.2 ± 0.3	15.5 ± 0.9	11.0 ± 1.1	13.3 ± 0.2
	Cellpose	17.1 ± 0.4	9.9 ± 0.7	17.5 ± 0.4	9.6 ± 1.6	17.9 ± 0.3	18.0 ± 0.7	8.9 ± 1.5	13.2 ± 0.3	10.3 ± 0.7	12.4 ± 0.8	14.3 ± 1.6	8.6 ± 0.3	10.8 ± 0.5
span	Laser	1.50 ± 0.04	1.96 ± 0.09	1.49 ± 0.02	2.06 ± 0.05	1.46 ± 0.03	1.47 ± 0.00	1.94 ± 0.03	1.61 ± 0.07	1.75 ± 0.04	1.69 ± 0.04	1.60 ± 0.05	1.82 ± 0.07	1.67 ± 0.04
	Watershed	0.80 ± 0.03	1.32 ± 0.37	0.78 ± 0.01	1.37 ± 0.49	0.81 ± 0.03	0.81 ± 0.01	1.15 ± 0.60	0.82 ± 0.02	1.08 ± 0.06	0.89 ± 0.01	0.84 ± 0.01	1.12 ± 0.10	1.11 ± 0.18
	Cellpose	0.79 ± 0.01	1.14 ± 0.03	0.88 ± 0.06	1.49 ± 0.37	0.78 ± 0.03	0.83 ± 0.02	1.12 ± 0.21	0.84 ± 0.03	0.96 ± 0.04	0.87 ± 0.03	0.91 ± 0.04	0.86 ± 0.01	0.98 ± 0.03

The dv90 is higher with the laser. At ×10, the laser dv90 exceeds the Cellpose value on 12 of the 13 samples, by 18 to 19% on average over the three magnifications. The only exception is E4, whose dv90 at ×10 is the least reproducible value in the table. The watershed follows the same trend on the coarse samples. On the fine samples, its dv90 is too dispersed to be interpreted (up to ±5.2 µm). Processing the laser data with the non-spherical particle analysis mode of the instrument software left dv10 and dv90 unchanged, so the shape assumption of the inversion does not explain the difference. Nor is the microscopy dv90 limited by statistics. At ×10, it rests on 98,500 to 286,288 droplets per sample; its between-slide standard deviation stays close to 1 µm on most samples, and the gap with the laser goes in the same direction on 12 of the 13 samples. The difference may arise on the laser side, but this remains a hypothesis that our data do not demonstrate. The regularized inversion may smooth and broaden the distribution, which would raise dv90 and lower dv10, in line with a laser span nearly twice that of microscopy. The sample may also evolve in the dispersion unit under dilution and stirring: $D[3,2]$ is highest in the first trial on all 13 samples, which shows that the dispersed sample is not static in the cell. Microscopy, in addition, shows large irregular objects on E3, E5′1, E5′2, E7, and E9 (Figure 3), which correspond to disordered lamellar domains rather than droplets, and measures them directly from their projected area. These explanations remain hypotheses. A dilution series on the laser measurement and a direct observation of the diluted sample would be needed to test them, and they were not performed here.

The De Brouckere mean $D[4,3]$ follows the dv90. It weights each droplet by its volume and is therefore sensitive to the coarse fraction. At ×10, the Cellpose $D[4,3]$ falls within 10% of the laser on 10 of the 13 samples. It is slightly lower on most of them, consistent with the higher laser dv90. The three exceptions are E4 (+13%), E11 (−27%), and E7, where one laser trial reads 28.4 µm against about 13 µm for the other two. This single trial shows how strongly a few large objects can shift a volume-weighted mean. The watershed departs more from the laser, 11 to 15% below it on the coarse samples and 15 to 23% above it on the fine ones.

The laser distribution is wider than the microscopy one. At ×10, its span lies between 1.46 and 2.06, against 0.78 to 1.49 for the two segmentations. The difference has a distinct cause at each end of the distribution. At the upper end, the laser dv90 is higher, possibly because of the smoothing of the inversion and of the evolution of the sample under dilution. The single refractive index of the Mie model, which ignores the anisotropic lamellar shell, may also contribute. At the lower end, the microscopy dv10 is higher because microscopy does not detect droplets below its resolution limit.

The three techniques are reproducible. The laser dv50 varies by 1.0% between trials, and the between-slide standard deviation of the microscopy dv50 stays below 1 µm in 36 of the 39 sample and magnification pairs for both segmentations.

The conversion from two to three dimensions remains the main limit of the image route, because the cube amplifies any error in the diameter. Droplets slightly flattened between the slide and coverslip would be overestimated for the same reason.

A natural question is whether a higher magnification would agree better with laser diffraction than the ×10 reported here. We compared each magnification on its own with the laser, using the median absolute deviation between Cellpose and the laser over the thirteen samples (Table 7).

No single magnification is best on every descriptor (Table 7). The ×10 is closest on the central size (dv50, 0.31 µm) and on dv10 and $D[4,3]$. The ×20 improves only the dv90, where it reaches 3.94 µm against 4.30 µm at ×10. The ×40 is best on the fine descriptors dv10 and $D[3,2]$, because it resolves small droplets, but it is the worst on dv90.

Table 7. Median absolute deviation between Cellpose and laser diffraction (µm), per magnification, over the thirteen samples. Lower means closer agreement; the smallest value in each row is in bold.

Descriptor	×10	×20	×40
dv10	4.08	4.18	**3.16**
dv50	**0.31**	0.58	0.37
dv90	4.30	**3.94**	4.55
$D[3,2]$	4.08	4.07	**3.40**
$D[4,3]$	**0.98**	1.28	1.21

The pattern follows the trade-off between resolution and field of view. A higher magnification resolves finer droplets but images a smaller field, so it samples the coarse tail poorly and its dv90 is low. A lower magnification samples the tail better and reads the central size closest to laser diffraction. The ×20 sits between the two. It is not clearly better than ×10 on any descriptor except the dv90. Moving from ×10 to ×20 would trade a small gain on dv90 for a larger loss on dv10, dv50, and $D[4,3]$. We therefore report the ×10, which best matches the volume-central descriptors, and we attribute the residual dv90 difference to the broadening of the laser inversion, common to the three magnifications.

The agreement was quantified with paired tests (Section 2.6, Table 8). For Cellpose, the dv50 differs from the laser value by +2.0% at ×10 (adjusted $p = 0.13$) and by +2.8% at ×40 ($p = 0.45$). The +5.2% difference at ×20 is the only significant one ($p = 0.004$). At ×10, the Bland-Altman analysis gives a bias of +3.6% on the dv50, with limits of agreement from −11 to +20% (Figure S1). The watershed overestimates the dv50 by 17.2% at ×10 and by 12.8% at ×20, both significant, with a bias of +15.4% and limits from −5 to +41% at ×10. At ×40, its dv50 does not differ significantly from the laser (−1.5%, $p = 0.83$), but its dv90 and $D[4,3]$ are 27% and 15% lower, consistent with the failure of its seeding at that magnification.

Table 8. Paired comparison of microscopy with laser diffraction over the thirteen emulsions. Median relative difference to the laser (%) and Holm-adjusted p value in brackets (exact two-sided Wilcoxon signed-rank test, 15 comparisons per segmentation). Positive values mean larger sizes in microscopy. Values in bold: adjusted $p < 0.05$.

Descriptor	Cellpose			Watershed		
	×10	×20	×40	×10	×20	×40
dv10	**+133.8 (0.004)**	**+157.6 (0.004)**	**+129.4 (0.004)**	**+138.2 (0.004)**	**+175.3 (0.004)**	**+147.1 (0.004)**
dv50	+2.0 (0.13)	**+5.2 (0.004)**	+2.8 (0.45)	**+17.2 (0.004)**	**+12.8 (0.004)**	−1.5 (0.83)
dv90	**−18.5 (0.004)**	**−17.1 (0.004)**	**−23.1 (0.004)**	−10.0 (0.27)	**−10.0 (0.004)**	**−26.9 (0.004)**
$D[3,2]$	**+61.2 (0.004)**	**+61.2 (0.004)**	**+52.7 (0.004)**	**+71.6 (0.004)**	**+74.6 (0.004)**	**+49.3 (0.004)**
$D[4,3]$	−5.3 (0.054)	−6.7 (0.054)	**−11.3 (0.004)**	−1.7 (0.83)	−2.3 (0.82)	**−15.0 (0.004)**

The tails and the moments differ more (Table 8). Both segmentations give a higher dv10 (+129 to +175%) and a higher $D[3,2]$ (+49 to +75%) than the laser at every magnification, and Cellpose gives a lower dv90 (−17 to −23%); all these differences are significant after correction ($p = 0.004$). The Cellpose $D[4,3]$ is 5 to 11% lower than the laser value, significantly so at ×40 only ($p = 0.004$; $p = 0.054$ at ×10 and ×20). The agreement therefore holds for the central size and not for the ends of the distribution.

Emulsion E7 includes one laser trial whose $D[4,3]$ is driven by a single scan with a transient coarse mode (Section 3.1). This trial was flagged by its disagreement with the two other trials and traced to that scan; no formal outlier rule was applied, and no data were removed, so E7 enters the analysis with its mean over the three trials. Repeating the paired tests without E7 does not change the conclusions.

Two limits of this comparison should be stated. First, the Cellpose segmentation was not validated against a quantitative manual reference. The manual annotation of Section 3.2.3 is too small to give stable volume percentiles; it consists of fitted circles rather than pixel masks (so mask-overlap metrics cannot be derived), and extending it to the whole dataset was not feasible. The segmentation is supported instead by the independent agreement of its dv50 with laser diffraction. Second, all 13 emulsions derive from a single lamellar base formulation, so the results apply to lamellar emulsions of this type.

In summary, laser diffraction and Cellpose agree on the central droplet size of these lamellar emulsions. The watershed reaches this agreement on the coarsest samples only. The two techniques differ at the ends of the distribution, and each difference has a possible cause. The laser detects more fine droplets because it covers the submicron range. Microscopy reads a lower dv90, possibly because the laser inversion broadens the distribution and the sample evolves under dilution. The two techniques are therefore complementary. Laser diffraction is the only one that reaches the fine fraction. Microscopy with deep-learning segmentation is the more direct route for the coarse fraction of a lamellar emulsion, and it shows the objects it measures.

3.4. Lamellar Shell Under Polarized Light

Under crossed polarizers, the droplets of every sample appear bright on a dark field (Figure 6). Most of them show a Maltese cross, the optical signature of a concentric lamellar shell around the oil core. This observation confirms the lamellar organization of the emulsions and the core-shell structure of their droplets. Laser diffraction cannot resolve this structure, whereas the microscopy route images it on the same samples it sizes.

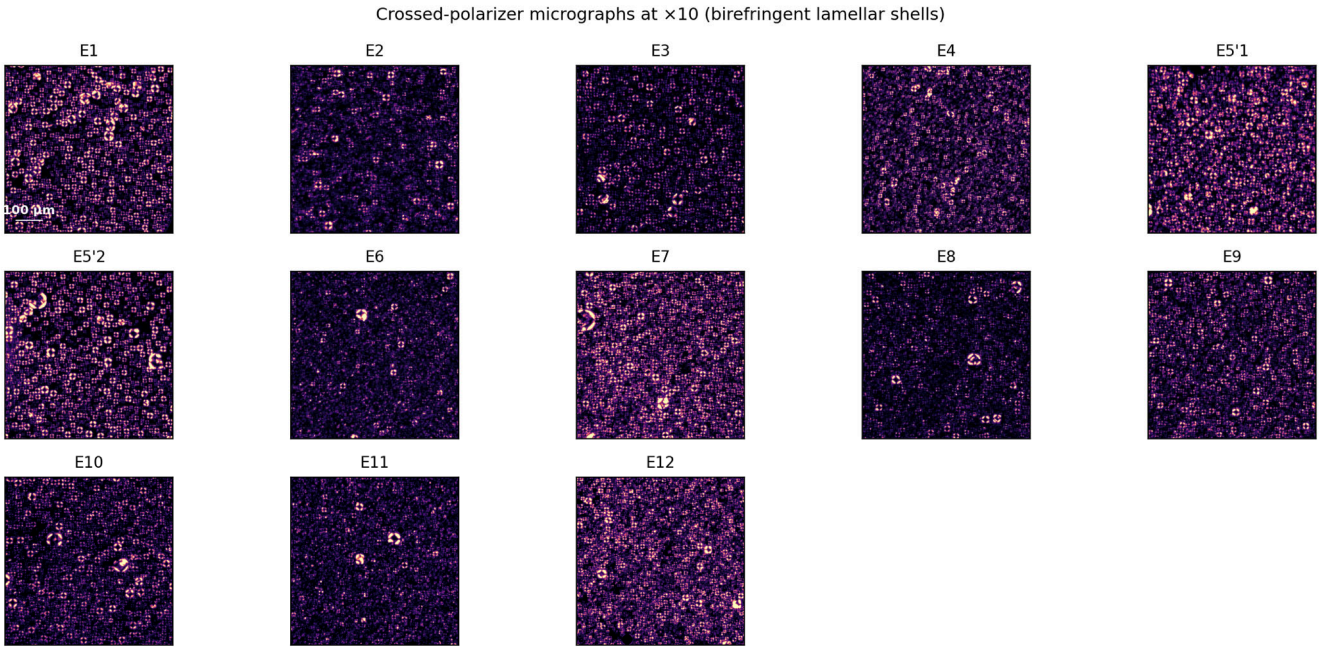

Figure 6. Crossed-polarizer micrographs (×10) of the 13 samples: birefringent lamellar shells appear bright (Maltese crosses). Contrast stretched for display. Intensity is shown in a false-color scale from dark (low) to bright (high). One panel per sample (E1 to E12; E5′1 and E5′2 included). (E1) 1000 rpm, 5 min; (E2) 3000 rpm, 5 min; (E3) 1000 rpm, 15 min; (E4) 3000 rpm, 15 min; (E5′1) 1000 rpm, 10 min; (E5′2) 1000 rpm, 10 min; (E6) 3000 rpm, 10 min; (E7) 2000 rpm, 5 min; (E8) 2000 rpm, 15 min; (E9) 2000 rpm, 10 min; (E10) 1567 rpm, 8.75 min; (E11) 2433 rpm, 8.75 min; (E12) 2000 rpm, 12.5 min (process conditions as in Table 1). Scale bar: 100 µm (E1 panel; same scale in all panels).

4. Conclusions

This study compared laser diffraction and optical microscopy for sizing the droplets of a lamellar cosmetic emulsion. On a common volume-weighted basis, thirteen samples covering a dv50 range from 6.5 to 16.9 µm were compared. The images were acquired at ×10, ×20, and ×40 and segmented by a classical watershed and by a deep-learning model (Cellpose).

Cellpose and laser diffraction converge on the central size. For lamellar emulsions, whose birefringent shell has no single, well-defined refractive index, this convergence of two independent techniques gives confidence in the central size measured by both. Their dv50 differ by less than 1.5 µm on every sample at ×10, and by at most 1.6 µm across the three magnifications. Paired tests confirm this: the Cellpose dv50 does not differ significantly from the laser value at ×10 and ×40 (+2.0 and +2.8%) and is 5.2% higher at ×20 (Table 8). The watershed does not reach the same level. It agrees with the laser on the coarsest samples only. On the finer samples, it overestimates the dv50 by 15 to 35%, and it fails at ×40. Among the magnifications, ×10 gives the closest agreement with laser diffraction on the central size. The ×40 objective resolves finer droplets but samples the coarse tail poorly.

The two techniques differ only at the ends of the distribution, and each difference has a possible origin. At the upper end, the laser dv90 and $D[4,3]$ are higher. This difference is not removed by a non-spherical particle model and possibly comes from the smoothing of the laser inversion and from the evolution of the sample under dilution. Microscopy, by contrast, measures the coarse droplets directly on the image, on 98,500 to 286,288 droplets per sample. At the lower end, the situation is reversed. The microscopy dv10 and $D[3,2]$ are higher because droplets below the optical resolution are not detected. For this fine fraction, laser diffraction remains the method of choice. These differences in dv10, dv90, and $D[3,2]$ are significant after correction (Table 8), so the agreement holds for the central size and not for the tails of the distribution. The proposed explanations for the dv90 are hypotheses; a dilution series on the laser measurement would test them.

Beyond size, microscopy also gives access to the structure of the droplets. Under crossed polarizers, Maltese crosses are observed on every sample. They confirm the lamellar shell that the laser model ignores and that laser diffraction cannot resolve.

These results have limits. The two techniques do not measure the same quantity. Laser diffraction derives a volume-weighted distribution from the light scattered by droplets dispersed in three dimensions. Microscopy, in contrast, measures the projected outline of each droplet in two dimensions. Its number-based diameters were therefore converted to volume by assuming spherical droplets. The agreement on the central size was also obtained on a single base formulation, so the refractive-index contrast between oil, shell, and water was not varied. The conclusions therefore apply to lamellar emulsions of this type and remain to be tested on other emulsifiers and on non-lamellar emulsions. In addition, the Cellpose segmentation was not validated against a quantitative manual reference, so its validation rests on the agreement of the dv50 with laser diffraction.

Finally, both techniques rank the samples in the same order with respect to the homogenization conditions. Taken together, these results make microscopy with Cellpose segmentation a promising tool for sizing lamellar emulsions of this type. It is well suited to industrial use, since it requires only standard laboratory equipment and no retraining of the model, and it combines sizing and structural observation on the same slide. In practice, image analysis needs only a standard optical microscope, a small amount of sample and a GPU for the Cellpose inference (the passes are stored and reused), and it gives droplet-by-droplet data and a view of the lamellar shell, whereas laser diffraction remains the faster and more repeatable choice for the routine control of the whole distribution. It can therefore support the characterization of lamellar emulsions during formulation and process

development. For the lamellar structure itself, it is complementary to transmission electron microscopy and X-ray scattering: polarized microscopy reveals the lamellar organization at the droplet scale, transmission electron microscopy images the lamellar layers, and small- and wide-angle X-ray scattering (SAXS and WAXS) resolve the lamellar spacing and the packing of the alkyl chains at the nanometer scale [10,26,27].

Supplementary Materials: The following supporting information can be downloaded at: https://www.mdpi.com/article/10.3390/cosmetics13060323/s1, Figure S1. Bland-Altman plots of Cellpose and watershed against laser diffraction at ×10 (log ratio; percent bias and limits of agreement).

Author Contributions: Conceptualization, A.V., R.C. and B.A.; methodology, A.V. and P.P.; software, A.V.; formal analysis, A.V., M.C.-B. and C.S.; investigation, A.V. and P.P.; resources, B.A.; data curation, A.V.; writing—original draft, A.V.; writing—review and editing, A.V., R.C., M.C.-B. and C.S.; visualization, A.V. All authors have read and agreed to the published version of the manuscript.

Funding: This research was funded by SICAF Cosmétiques, as part of a collaboration with the Faculty of Pharmacy and the Faculty of Sciences of Aix-Marseille University.

Institutional Review Board Statement: Not applicable.

Informed Consent Statement: Not applicable.

Data Availability Statement: Data will be made available on request.

Acknowledgments: The project is the result of a collaboration between the Faculty of Pharmacy of Aix-Marseille University, the Faculty of Sciences of Aix-Marseille University, and the company SICAF, which funded the project. During the preparation of this work, the authors used Claude Sonnet 5 (Anthropic) for language editing and readability improvements, manuscript structuring, and verification and formatting of bibliographic references. The authors reviewed and edited the output as needed and take full responsibility for the content of the published article.

Conflicts of Interest: The authors declare that this research was funded by SICAF, with which two of the authors (Axel Viton and Béatrice Anthouard) are affiliated. The authors declare no other competing financial interests or personal relationships that could have influenced the work reported in this paper.

Abbreviations

The following abbreviations are used in this manuscript:

DSD	Droplet size distribution
LD	Laser diffraction
NA	Numerical aperture
PDPA	Phase Doppler particle analysis
SAXS	Small-angle X-ray scattering
WAXS	Wide-angle X-ray scattering

References

1. Benito, J.M.; Ríos, G.; Pazos, C.; Coca, J. Droplet size distribution of oil–water emulsions by confocal laser scanning microscopy. In *Particle Sizing and Characterization*; Provder, T., Texter, J., Eds.; ACS Symposium Series 881; American Chemical Society: Washington, DC, USA, 2004; pp. 75–88. [CrossRef]
2. McClements, D.J. *Food Emulsions: Principles, Practices, and Techniques*, 3rd ed.; CRC Press: Boca Raton, FL, USA, 2015.
3. Milanković, V.; Krstonošić, V.; Lukić, M. Not just water: Ionic influence on the rheology of natural O/W emulsions. *J. Chem. Technol. Biotechnol.* **2025**, *101*, 578–589. [CrossRef]
4. *ISO 13320:2020*; Particle Size Analysis. Laser Diffraction Methods. International Organization for Standardization: Geneva, Switzerland, 2020.
5. Arganda-Carreras, I.; Kaynig, V.; Rueden, C.; Eliceiri, K.W.; Schindelin, J.; Cardona, A.; Seung, H.S. Trainable Weka Segmentation: A machine learning tool for microscopy pixel classification. *Bioinformatics* **2017**, *33*, 2424–2426. [CrossRef]

6. van der Walt, S.; Schönberger, J.L.; Nunez-Iglesias, J.; Boulogne, F.; Warner, J.D.; Yager, N.; Gouillart, E.; Yu, T. scikit-image: Image processing in Python. *PeerJ* **2014**, *2*, e453. [CrossRef]
7. Stringer, C.; Wang, T.; Michaelos, M.; Pachitariu, M. Cellpose: A generalist algorithm for cellular segmentation. *Nat. Methods* **2021**, *18*, 100–106. [CrossRef]
8. Pachitariu, M.; Stringer, C. Cellpose 2.0: How to train your own model. *Nat. Methods* **2022**, *19*, 1634–1641. [CrossRef]
9. Chng, C.-P.; Gupta, S.; Huang, C. Effect of surfactant-fatty alcohol ratio on physico-mechanical properties of lamellar gel phase bilayers. *npj Soft Matter* **2026**, *2*, 3. [CrossRef]
10. Eccleston, G.M.; Behan-Martin, M.K.; Jones, G.R.; Towns-Andrews, E. Synchrotron X-ray investigations into the lamellar gel phase formed in pharmaceutical creams prepared with cetrimide and fatty alcohols. *Int. J. Pharm.* **2000**, *203*, 127–139. [CrossRef]
11. Dallay, C.; Malhiac, C.; Duchemin, B.; Savary, G.; Picard, C. Effect of linalool on lamellar-structured emulsions: From molecular organization to organoleptic properties. *Food Hydrocoll.* **2024**, *149*, 109575. [CrossRef]
12. Chanpirom, S.; Tree-Udom, T.; Inchai, P.; Krongthamsiri, P.; Yodsing, C.; Chantapa, S.; Narupabenjapon, V.; Saewan, N.; Ditthawutthikul, N.; Vinardell, M.P.; et al. Effective skin hydration using an ultra-micro liquid crystal emulsion containing pumpkin seed oil and polysaccharides. *Cosmetics* **2026**, *13*, 49. [CrossRef]
13. Fameau, A.-L.; Veronico, L.; Le Coeur, C.; Mahmoudi, N.; Gentile, L. Shear and cooling effects on lamellar gel network structure: Insights from Rheo-SANS. *J. Mol. Liq.* **2024**, *414*, 126283. [CrossRef]
14. Teeranachaideekul, V.; Soontaranon, S.; Sukhasem, S.; Chantasart, D.; Wongrakpanich, A. Influence of the emulsifier on nanostructure and clinical application of liquid crystalline emulsions. *Sci. Rep.* **2023**, *13*, 4185. [CrossRef]
15. Savić, S.; Lukić, M.; Jaksić, I.; Reichl, S.; Tamburić, S.; Müller-Goymann, C.C. An alkyl polyglucoside-mixed emulsifier as stabilizer of emulsion systems: The influence of colloidal structure on emulsions skin hydration potential. *J. Colloid Interface Sci.* **2011**, *358*, 182–191. [CrossRef]
16. Salum, P.; Güven, O.; Aydemir, L.Y.; Erbay, Z. Microscopy-assisted digital image analysis with Trainable Weka Segmentation (TWS) for emulsion droplet size determination. *Coatings* **2022**, *12*, 364. [CrossRef]
17. Verveld, W.; de Wolf, J.R.; Legtenberg, C.G.; Knop, T.; Bosschaart, N. Human milk fat globule size distributions: Comparison between laser diffraction and 3D confocal laser scanning microscopy. *Food Res. Int.* **2024**, *198*, 115282. [CrossRef]
18. Khosravi, H.; Thaker, A.H.; Donovan, J.; Ranade, V.; Unnikrishnan, S. Artificial intelligence and classic methods to segment and characterize spherical objects in micrographs of industrial emulsions. *Int. J. Pharm.* **2024**, *649*, 123633. [CrossRef]
19. Saalbrink, J.; Loo, T.Y.J.; Mertesdorf, J.; Xu, P.; Pedersen, M.T.; Clausen, M.P.; Bonilla, J.C. Quantifying microscopic droplets in colloidal systems through machine learning-based image analysis. *Food Hydrocoll.* **2025**, *166*, 111301. [CrossRef]
20. Zhang, S.; Liang, X.; Huang, X.; Wang, K.; Qiu, T. Precise and fast microdroplet size distribution measurement using deep learning. *Chem. Eng. Sci.* **2022**, *247*, 116926. [CrossRef]
21. Burke, I.; Dhayaparan, T.; Youssef, A.S.; Schmidt, K.; Kockmann, N. Two deep learning methods in comparison to characterize droplet sizes in emulsification flow processes. *J. Flow Chem.* **2024**, *14*, 597–613. [CrossRef]
22. Bana, G.; Lamadie, F.; Charton, S.; Randriamanantena, T.; Lucor, D.; Sheibat-Othman, N. BYG-drop: A tool for enhanced droplet detection in liquid–liquid systems through machine learning and synthetic imaging. *Front. Chem. Eng.* **2024**, *6*, 1415453. [CrossRef]
23. Sijs, R.; Kooij, S.; Holterman, H.J.; van de Zande, J.; Bonn, D. Drop size measurement techniques for sprays: Comparison of image analysis, phase Doppler particle analysis, and laser diffraction. *AIP Adv.* **2021**, *11*, 015315. [CrossRef]
24. Beucher, S.; Meyer, F. The morphological approach to segmentation: The watershed transformation. In *Mathematical Morphology in Image Processing*; Dougherty, E.R., Ed.; Marcel Dekker: New York, NY, USA, 1993; pp. 433–481.
25. Stringer, C.; Pachitariu, M. Cellpose3: One-click image restoration for improved cellular segmentation. *Nat. Methods* **2025**, *22*, 592–599. [CrossRef]
26. Ahmadi, D.; Mahmoudi, N.; Li, P.; Ma, K.; Doutch, J.; Foglia, F.; Heenan, R.K.; Barlow, D.; Lawrence, M.J. Revealing the hidden details of nanostructure in a pharmaceutical cream. *Sci. Rep.* **2020**, *10*, 4082. [CrossRef]
27. Savić, S.; Vuleta, G.; Daniels, R.; Müller-Goymann, C.C. Colloidal microstructure of binary systems and model creams stabilized with an alkylpolyglucoside non-ionic emulsifier. *Colloid Polym. Sci.* **2005**, *283*, 439–451. [CrossRef]

Disclaimer/Publisher's Note: The statements, opinions and data contained in all publications are solely those of the individual author(s) and contributor(s) and not of MDPI and/or the editor(s). MDPI and/or the editor(s) disclaim responsibility for any injury to people or property resulting from any ideas, methods, instructions or products referred to in the content.